Bandgap engineered smart three-terminal solar cell: New perspectives towards very high efficiencies in the silicon world

Zakaria Djebbour, Walid El-Huni, Anne Migan-Dubois, Jean-Paul Kleider

Full title :

Band gap engineered smart three terminal solar cell: new perspectives towards very high efficiencies in the silicon world

Short title :

Band gap engineered smart three terminal solar cell

Names and affiliations of all authors :

Zakaria Djebbour[1,2], Walid El-Huni[1], Anne Migan[1], Jean-Paul Kleider[1]

[1] GeePs ; CNRS UMR 8507 ; CentraleSupélec ; Univ Paris-Sud ; Sorbonne Université ; 11 rue Joliot-Curie, Plateau de Moulon, F-91192 Gif-sur-Yvette Cedex, France
[2] Département des Sciences Physiques, UVSQ, 45 avenue des Etats-Unis, 78035 Versailles, France

Corresponding author :

Zakaria Djebbour
Zakaria.djebbour@centralesupelec.fr
Telephone : +33 1 69 85 16 42
Fax : +33 1 69 41 83 18

Zakaria Djebbour[1,2], Walid El-Huni[1], Anne Migan[1], Jean-Paul Kleider[1]

[1] GeePs ; CNRS UMR 8507 ; CentraleSupélec ; Univ Paris-Sud ; Sorbonne Université ; 11 rue Joliot-Curie, Plateau de Moulon, F-91192 Gif-sur-Yvette Cedex, France
[2] Département des Sciences Physiques, UVSQ, 45 avenue des Etats-Unis, 78035 Versailles, France

Title :

Band gap engineered smart three terminal solar cell: new perspectives towards very high efficiencies in the silicon world

Abstract :

We present the design of a new architecture of three-terminal (3-T) photovoltaic tandem solar cells. It combines an interdigitated back contacted (IBC) bottom lateral subcell with a heterojunction vertical top cell. In this concept, the two subcells can work independently and there is no need for tunnel junctions. It is particularly well suited to silicon back contact subcells and to various types of top cell materials from III-V compounds or perovskites. The working principle is detailed here using as an example a p/i III-V front stack onto n-type silicon IBC bottom cell. We perform 2D modeling using realistic material input parameters and show how interface bandgap engineering can improve the tandem cell efficiency up to a reachable 35% value. The proposed cell concept named BESTT (bandgap engineered smart silicon three-terminal) cell can be realized with less technological steps and at a lower cost compared to the conventional four-terminal process.

I. Introduction

Today, 94% of the steadily increasing photovoltaic (PV) market is based on silicon (Si). Laboratory Si solar cells have reached a maximum power conversion efficiency (PCE) above 26 % [1]. This is already close to the Shockley-Queisser theoretical limit of about 32% for a single junction cell [2] and even closer to the practical limit of about 29% for a silicon cell when the intrinsic Auger recombination is taken into account [3]. Hence, further significant breakthrough in silicon based solar cells is only possible with the addition of other ingredients and concepts like that of multijunctions. As a matter of fact, nowadays world record solar cells' efficiency is achieved with multijunction solar cells based on III-V compounds [4].

Two main architectures of multijunctions have been proposed: monolithic 2-terminal, and 4-terminal cells [5]. Due to current-matching and lattice-matching conditions, material choices are limited for monolithic multijunction solar cells. For instance, the triple-junction InGaP/InGaAs/Ge solar cell achieved by SpectroLab [6], with an efficiency of 41.6%, has all the junctions lattice-matched, but they do not have the optimal bandgap combination. Other groups have tried to respect the current-matching condition using metamorphic growth where the slight lattice mismatch between materials is adapted using graded buffer layers. However, lattice-mismatch still induces dislocation defects that tend to extend through the epitaxied layers causing a degradation in performance, as it is the case in the triple-junction monolithic InGaP/GaAs/InGaAs cell achieved by Takamoto et al. [7]. For dual-junction (tandem) solar cells, the theoretical radiative limit efficiency is 42% under AM1.5G conditions[8,9], while the maximum conversion efficiency achieved today is 31.6% with the GaInP/GaAs stack [10] that does not have the optimum bandgap combination and uses a costly GaAs substrate. Dimroth et al. [11] have studied the direct growth of GaAs on low-cost silicon substrates using a GaAsP metamorphic buffer layer. Tanabe et al. [12] have demonstrated an AlGaAs/Si tandem cell using a direct bonding technique. They have achieved a PCE of 25.2%. Progress in bonding techniques have also lead to a recent record PCE of 30.2% in a monolithic two-terminal triple-junction III-V/Si cell [13]. As III-Nitrides are less expensive than III-Phosphides and III-Arsenides, Reichertz et al. [14] have studied the combination of high-bandgap GaN material onto Si for a low-cost tandem

cell, reaching open circuit voltages of 2.5V but very poor current matching. Perovskites are also considered as low-cost and potentially suitable materials to be coupled to silicon, and record efficiencies for monolithic perovskite/silicon cells are approaching 25% [15].

Liu et al. [16] have shown that the yield of a 4-terminal tandem cell is more than 15% higher than for a 2-terminal one, because the 4-terminal design does not require current matching between subcells. Yang et al. [17] have shown that the Si-based bottom subcell in 3-junction InGaP/GaAs/Si cells produces 35% less short-circuit current compared to the theoretical expected maximum value achievable for a silicon bottom cell filtered by an InGaP/GaAs 2-J stack. Record cell efficiencies in the 4-terminal configuration for III-V/Si cells reach 32.8% for two junctions and 35.9% for three junctions, respectively [18], while 4-terminal perovskite / Si tandem cells above 25% have been obtained [19].

Three-terminal (3-T) cells have been only poorly studied so far. Some early work on 3-T structures using an interdigitated back contact cell has been proposed by Nagashima et al. [20,21], while J. C. Jimeno et al. more recently studied a possible connection scheme of 3-T cells [22]. In 2015 A. Marti and A. Luque made a theoretical investigation of a 3-T heterojunction bipolar transistor solar cell (HBTSC) with stacked layers of alternate doping (n-Emitter, p-Base, and n-Collector, with the emitter and base made of a large bandgap compared to the lower bandgap collector), showing that the detailed balance efficiency limit is the same as for a standard type double-junction solar cell [23]. However, no concrete solution for the realization of such a HBTSC was proposed.

Recent works on 3-T have been published where the carrier selectivity is provided by a tunnel junction [22], by nanoscale back contacts on the top cell [24], or by a selective electrode in the top cell [5]. Our suggestion is to use the heterojunction to provide the selectivity as we can see later in this work. Bandgap engineering at the heterointerface can provide such a selectivity, in particular with the addition of a selective barrier layer made of engineered band offsets.

In this paper, we propose a 3-T cell architecture that uses an IBC silicon bottom cell combined with a top front heterojunction stack (FHS) cell where a specific band offset offers a selective carrier flow at the heterointerface with silicon. This type of solar cells that we have patented [25] will be called here the BESTT (bandgap engineered smart silicon three-terminal) cell. We demonstrate the operation principle of such a cell and calculate the improved performance that can be expected thanks to suitable band offset management between the top absorber material and the bottom silicon cell.

II. 3-T architecture

The schematic view of the proposed 3-T architecture is shown in Figure 1 for either n- or p-type silicon absorber. More generally, the top cell can be made of a stack of layers, the FHS (p-FHS or n-FHS), but the interface with silicon has to be chosen in order to form a selective heterojunction for one type of carriers, enabling the separation of the operation of the two subcells. This can be favored by introducing a selective barrier layer made of engineered band offsets will be described hereafter, which we call Selective Layer (SL) in this work. We here develop the working principle and calculations for a bottom IBC with an n-type absorber, and a p-type FHS (Figure 1a) (it can be straightforward adapted to a p-type based IBC and n-type front FHS like in Figure 1b). The p-FHS and SL stacks can be obtained either by direct growth on the upper surface c-Si of the bottom cell, or by growth on a suitable substrate, followed by a dry or a chemical lift-off and a gluing on the upper face of c-Si (wafer bonding). The p-FHS stack can form a p-i-n diode with the n-type silicon wafer and make use of a front surface field for enhanced hole extraction to the front electrode. This p-FHS/n-silicon top sub cell heterojunction differs fundamentally from top sub cells used in Adhyaksa et al. and Warren et al. works, since in our case, the top sub cell uses the IBC n-silicon substrate to form the p-i-n heterojunction. The absorbing i-layer must have a bandgap greater than that of silicon, the optimum value being between 1.6 and 2 eV, with an optimum at 1.81 eV taking into account the band gap of the silicon (1.12 eV) [26].

III. Principle of operation of the BESTT cell

We have used ATLAS module of SILVACO TCAD to perform the electrical and optical simulations, choosing transfer matrix method (TM) for the photogeneration. The details of the parameters for both the FHS and the bottom cell are not described here. We have used for instance, Adachi's dispersive model for the refractive index in GaInP [27], Caughey-Thomas's model which takes into account the doping and temperature dependence of carrier mobilities [28], and concentration dependent Shockley-Read-Hall recombination model in silicon [29,30].

a. Simulation parameters

Table 1 summarized some of the FHS parameters used in our calculations. All the parameter's values in this table have been taken from the literature [31,32,33,34,35]. IBC cell and GaN layer parameters, taken from the literature [36] and [37] respectively, are summarized in Table 2. SRV is the surface recombination velocities. Schokley-Read-Hall (SRH) recombination has been considered :

$$R_{SRH} = \frac{np - n_i^2}{\tau_n^{SRH}\left[n + n_i exp\left(\frac{E_{trap}}{kT}\right)\right] + \tau_p^{SRH}\left[p + n_i exp\left(-\frac{E_{trap}}{kT}\right)\right]}$$

with, n and p, the electrons and holes concentrations, τ_n^{SRH} and τ_p^{SRH}, the doping level dependent electrons and holes life times respectively, n_i the intrinsic concentration, E_{trap} the trap level in the bandgap, k the Boltzmann constant and T the absolute temperature. τ_n^{SRH} and τ_p^{SRH} are respectively given by :

$$\tau_n^{SRH} = \frac{\tau_{n_0}^{SRH}}{A_n + B_n\left(\frac{N_{total}}{N_n^{SRH}}\right) + C_n\left(\frac{N_{total}}{N_n^{SRH}}\right)^{E_n}}$$

$$\tau_p^{SRH} = \frac{\tau_{p_0}^{SRH}}{A_p + B_p\left(\frac{N_{total}}{N_p^{SRH}}\right) + C_p\left(\frac{N_{total}}{N_p^{SRH}}\right)^{E_p}}$$

where N_{total} is a net doping concentration, $\tau_{n_0}^{SRH}$ and $\tau_{p_0}^{SRH}$ are the initial life times, $A_{n,p}$ $B_{n,p}$, $C_{n,p}$, $E_{n,p}$ and $N_{n,p}^{SRH}$ are fit parameters, summarized in Table 2.

Auger recombination has also been taken into account. It is expressed as :

$$R_{Auger} = C_{Aug}^n n(np - n_i^2) + C_{Aug}^p p(np - n_i^2)$$

where C_{Aug}^n and C_{Aug}^p are Auger recombination coefficients of electrons and holes respectively.

The total recombination is the sum of R_{SRH} and R_{Auger}. Radiative recombination R_{rad} has been neglected in case of silicon absorber.

Concerning carrier mobilities, we have used Caughey-Thomas model which takes into account doping temperature dependencies of mobilities and can be simplified at $T = 300\ K$ as :

$$\mu_{n,p} = \mu_{1_{n,p}} + \frac{\mu_{2_{n,p}} - \mu_{1_{n,p}}}{1 + \left(\frac{N_{total}}{N_{n,p}^{ref}}\right)^{\delta_{n,p}}}$$

where μ_1, μ_2, δ and N^{ref} are fit parameters summarized in Table 2.

b. Cell simulations

We have chosen the material parameters to be compatible with literature data [36,38] and to reproduce realistic photovoltaic performance of the individual subcells. As an individual top cell, we have considered the FHS/n-Si heterojunction with the n^+-Si back surface field (Figure 2a) and a top front

75 nm thick layer of Polymethylmethacrylate (PMMA). This type of coating has already been used in gallium phosphide photovoltaic junctions as a cheap anti-reflecting layer [38]. The FHS stack is formed of a 20 nm thick p-type GaP window cap layer, a 50 nm thick intrinsic $Ga_xIn_{1-x}P$ with graded bandgap (between 2.35 eV down to 1.78 eV), and a 1 μm thick intrinsic $Ga_{0.35}In_{0.65}P$ absorber, the bandgap of which is 1.78 eV. The graded bandgap layer has been chosen in order to smooth the band offsets between the window layer and the absorber. As an individual bottom cell we have simulated the performance of the IBC cell, inspired by the cell studied at Australian National University's laboratories [36], without any front texturization, and with a front anti-reflection layers made of 90 nm thick SiO_2 and 65 nm thick SiN slabs (Figure 2b).

Table 3 summarizes the obtained simulated photovoltaic performances of the subcells. For the GaInP/Si based subcell, the simulated open circuit voltage and efficiency are lower compared to the record experimentally achieved in a GaInP single cell [39]. This is due in our cell to the heterojunction with silicon that reduces the open circuit voltage. On the other hand, our calculated short circuit current is slightly larger, which is due to the slightly lower bandgap taken here (1.78 eV) as compared to that of the record cell (1.81 eV). For the n-Si IBC cell our calculated open circuit voltage and fill factor are very close to the ones that were experimentally obtained [36]. We find a significantly lower short circuit current value due to the fact that the front surface of the IBC cell in our case has no texturization.

In order to illustrate the BESTT cell concept and to make a realistic calculation of the PCE we take the concrete example shown in Figure 3a. It combines an n-type crystalline silicon absorber IBC of Figure 2b example, without antireflecting coating, as a bottom-cell with a FHS stack of Figure 2a example as a top cell.

The band diagram at thermodynamic equilibrium of the corresponding stacks is given in Figure 3b. One can see that, owing to the almost aligned electron affinities between GaInP and Si there is no barrier for the electrons photogenerated in the top cell to pass into the silicon, and thus no thermalization losses. On the other hand, there is a valence band offset at the i-GaInP/n-Si heterointerface that makes a barrier for the holes photogenerated in silicon to pass into i-GaInP. Holes photogenerated in the i-GaInP absorber are drifted by the electric field towards the front interface. However, since they have no barrier at the heterointerface with silicon, some of them may diffuse into silicon where they thermalize, causing some electric losses. Later, we will see how the introduction of the SL layer, forming a barrier for holes in both directions while keeping no barrier fo electrons, can enhance the photovoltaic performance of the tandem solar cell.

Figure 4a shows the current mapping due to photogenerated electrons in the whole solar cell. One observes that electrons are extracted only at the back n-electrode. The strong electric field formed by the p-type FHS and the n-Si substrate drives the electrons that are photogenerated in the large bandgap layers into the silicon. This is emphasized by Figure 4b, which is an enlargement of a portion of Figure 4a, where it can be seen that the electron flow is almost vertical and that electrons cross smoothly the heterointerface thanks to the conduction band alignment. This, of course, is fully different from the behavior in the conventional 2-T IBC cell where there is no vertical current flow at the cell top surface. Here we have a combination of the flow of electrons drifting from the top large bandgap layers into the silicon with the electrons photogenerated in silicon, both diffusing in the n-Si to the collecting n-electrode. This yields the S-shape of the total electron flow observed in Figure 4a.

The same kind of S-shape is observed for the flow of holes when looking at the mapping in the whole structure (Figure 5a), due to the extraction of holes at the p-Si back contact, while no holes are extracted at the n-Si back contact. Most of the holes photogenerated in the upper large bandgap layers are driven by the electric field toward the front electrode as can be seen by the vertical flow lines in the upper part of Figure 5b. As observed in Figure 3b, the heterointerface between the large bandgap top layers and the silicon produces a barrier for the holes photogenerated in silicon to cross this interface, but there is no barrier for holes photogenerated in the large bandgap layer to cross the heterointerface and to enter into silicon. Consequently, holes photogenerated in the large bandgap InGaP layer close to the silicon interface diffuse into silicon, where they are then collected by the

back p-Si electrode. This is illustrated in Figure 5b, where the zoom at the heterointerface clearly shows that there is a horizontal demarcation line slightly above the heterointerface. This is the demarcation between holes that are driven by the electric field to the top electrode and those diffusing to the silicon. The latter are responsible for losses in the overall performance of the solar cell since they partly thermalize from the large bandgap top layer to the silicon.

In order to suppress these losses one can introduce a selective layer SL that produces a barrier for holes from the top layers to the silicon, while still allowing the photo-generated electrons to pass through. The choice of the material for the SL then depends on its bandgap and electronic affinity, compared to the low bandgap silicon and to the top large bandgap. For our example of Figure 3a, where the large bandgap is an GaInP alloy, one good candidate for the SL is GaN, the resulting BESTT structure being depicted in Figure 6a, where a 150 nm GaN layer has been introduced. Indeed, GaN has almost the same electron affinity as GaInP and Si, while having a significant band offset with both semiconductors of more than 2 eV, as shown in the energy band diagram at equilibrium of Figure 6b.

Figure 7a shows the holes current mapping at the interface between the SL layer and silicon. Comparing with Figure 5b, it can be observed that the SL layer has indeed suppressed the diffusion of holes from the large bandgap absorber to the silicon wafer. The demarcation line for holes is now located right at the i-GaInP/i-GaN interface. It has to be noted that photogeneration in the SL layer is negligible due to its very large bandgap. Figure 7b illustrates the total photocurrent density mapping (i.e. sum of electrons and holes) for the whole structure under AM1.5G and in the short-circuit condition. It emphasizes the combined action of both subcells, with a combination of vertical and lateral carrier extraction. The current density is larger close to the bottom n-Si electrode.
This is also a result of the n^+-Si back electrode region being smaller than the p^+-Si emitter back electrode, as is usually the case in IBC structures [36]. However the effect is more pronounced in the 3-T architecture because electrons photogenerated in both the top large bandgap layers and the bottom Si wafer are extracted at this electrode while photogenerated holes are extracted at either top or bottom p-electrodes, according to the photogeneration location.

c. Performance outlook

Figure 8 shows the mapping of power conversion efficiency of the BESTT cell without SL (Figure 8a) and with SL (Figure 8B) as a function of the voltage at each subcell. In the case of the BESTT cell without SL, the calculations show that the optimum of the top cell maximum power point voltage, $V_{mpp,top}$, occurs when the operation point voltage of the bottom cell, $V_{op,bot}$, is equal to 600 mV. On the other hand, the optimum of the bottom cell maximum power point voltage, $V_{mpp,bot}$, occurs when the operation point voltage of the top cell, $V_{op,top}$, is equal to 1.02 V. This value is significantly lower than the value obtained in a single GaInP cell, due to the thermalization of holes at the heterojunction with silicon. The best overall performance is obtained at the intercept with a total conversion efficiency of 27.2%.

Despite the thermalization losses, this is almost 3% (absolute) more than when the IBC cell is used separately and alone. Introducing the SL suppresses thermalization of holes, which is reflected in a larger value of the open circuit voltage of top the heterojunction cell (1.49 V instead of 1.13 V) and an increase to 1.32V of the voltage at the maximum power point. This leads to an increase of the overall power conversion efficiency to 31.7%, which now represents a gain of more than 7% absolute compared to the silicon IBC cell working alone. The efficiencies are limited in our calculations by the short circuit current values. Indeed, the sum of the short circuit currents of the two subcells amounts to 34.6 mA cm^{-2}, which is far below the 42 mA cm^{-2} obtained for the textured IBC cell alone. This is due to our choice of a Polymethylmethacrylate (PMMA) front antireflection layer, which is an easy low cost but unoptimized solution. If the reflection at the front surface is suppressed, our calculations show that the conversion efficiency increases to 35.0%.

The top and bottom subcells can be thought to be interdependent since they share the same n-type electron extracting electrode at the rear side. However, we demonstrate that the two subcells can

act independently from each other when the SL layer is introduced. To this purpose, for the two cases, without or with SL, we have simulated the I-V curves under AM 1.5G conditions for each subcell when the other subcell is maintained at a given operating point by fixing the voltage between its two electrodes.

Figure 9 shows the I-V curves under AM1.5G for each subcell when no SL is used. We note from Figure 9a that the I-V curves of the top cell are insensitive to the bottom cell operating point, $V_{op,bot}$ up to 0.6V. Beyond this value, the top cell experiences a slight increase of its open-circuit voltage. In the same way, Figure 9b shows that the I-V curves of the bottom cell are insensitive to the top cell operating point, $V_{op,top}$, up to 1V. Beyond this value, the bottom cell experiences a significant increase of its short-circuit current J_{SC}.

In order to explain and understand the slight increase of V_{OC} of the top cell on one hand, and the significant increase of J_{SC} of the bottom cell on the other hand, we use the vertical energy band diagram profiles from the top electrode to the bottom n-Si electrode under such operating conditions. In Figure 10a we present the profile for two operating points of the bottom cell, one close to short circuit and the other close to open-circuit, when the top cell is in the open-circuit condition. When the bottom cell operates close to its open circuit voltage rather than close to short circuit, the splitting of the quasi Fermi levels in the bottom cell is large. This is principally due to the increase of hole concentration but also to a slight increase of electron concentration, while the holes concentration in the large bandgap top layers remains almost unchanged, which leads to the slight increase in the open circuit voltage of the vertical heterojunction cell. In Figure 10b we present the band diagram from the top p-electrode to the bottom n-electrode when the bottom cell is in short circuit conditions, and for two values of the operating point of the top cell, one corresponding to short circuit, and the other one at 1.1 V, i.e. close to open circuit. In the latter case, the band bending in the wide bandgap upper layers is considerably lowered, so is the electric field. Holes photogenerated in the large bandgap layer are no longer simply drifting to the top electrode and hole diffusion becomes predominant. Thus a large part of these holes diffuse into the low bandgap material and can then be collected by the p-type back contact, which increases the bottom cell J_{SC}.

When varying Vop,bot and Vop,top, we obtain the Figure 8a that shows the mapping of PCE of the BESTT cell without SL as a function of the voltage at each subcell.

Figure 11 shows the I-V curves under AM1.5G for each subcell when the SL layer is introduced. If we compare with Figure 10, it is clear that each subcell of the tandem now operates fully independently from the other thanks to the SL layer: the I-V curve of one subcell does not depend on the voltage across the one other one. The total electric power of the BESTT cell is then simply the sum of the electric power of each subcell, as in a four-terminal tandem cell. Moreover, the SL layer prevents the diffusion of holes from the large bandgap top layer into the bottom silicon wafer even if the electric field collapses in the top layer, thus leading to a significant increase of the open circuit voltage of the top subcell compared to the case without SL layer (1.49V instead of 1.13V).

Figure 12 shows the best overall performances of the BESTT cell without (Figure 12a) and with (Figure 12b) the SL layer, and the corresponding I-V curves of the subcells.

IV. Conclusions and perspectives

We have proposed a three-terminal tandem cell combining a bottom silicon *lateral* IBC cell with a *vertical* top cell consisting in a heterojunction between the silicon wafer and a semiconductor or stack of semiconductors with larger bandgap on top of it and with a front top electrode. It can avoid some of the drawbacks encountered in conventional 2-T and 4-T cells, like current-matching, tunnel junctions or contact alignments. The working principle has been illustrated based on an n-type silicon absorber. In that case, on one hand, all photogenerated electrons, whether in the large bandgap top layers or in the silicon, have to be collected on the common n-electrode on the rear side. On the other hand, holes photogenerated in the large bandgap semiconductor stack have to be collected on the front electrode. Band gap engineering at the heterointerface is thus of great interest. Indeed, the conduction band edges of the top semiconductor and of silicon have to be aligned in order to avoid

either problems of electron transport or thermalization losses. If the conduction band is matched between materials, there will be a valence band offset that produces a barrier for holes from the silicon to the upper large bandgap semiconductor, while part of the holes generated in this upper semiconductor could flow into silicon, thus leading to thermalization losses. An additional selective band offset buffer layer, forming a barrier for the holes while having the conduction band aligned with both silicon and the upper larger bandgap semiconductor can then avoid such thermalization losses and lead to improved overall performance. We have proposed a full realistic simulation using a p-GaP/i-GaInP top stack, thus forming a vertical p-i-n heterojunction with silicon, and have demonstrated the benefit of introducing a GaN SL. We have shown that a gain of more than 7% in absolute efficiency values can be obtained compared to the single silicon IBC cells, leading to overall efficiencies of 32%. These are not idealized hypothetical efficiencies (as often given in the literature) but real efficiencies from complete simulations that take into account electronic transport and recombination mechanisms. Perspectives of efficiencies beyond 35% are open if reflection and non absorption losses issues can be solved. In additional simulations, we have replaced the GaN SL layer with a layer of ZnO, having an electronic affinity and a bandgap close to that of GaN, and we obtained almost the same photovoltaic performances (for a slightly thicker layer of ZnO: 200 nm instead of 150 nm for GaN).

While we have concentrated here on the working principle of a BESTT cell built on an n-type silicon wafer, the concept can be easily applied to a p-type silicon wafer. Also, the calculations have been performed here using a III-V compound as a top cell, but the absence of current matching requirement makes the BESTT structure very flexible and suitable to other choices of top materials like perovskites, so it opens a new route to high efficiency silicon based tandem solar cells.

Finally, the structure that we propose is especially interesting if it is possible to make a deposit or a direct growth on silicon. For the III-V the direct growth by Molecular Beam Epitaxy (MBE) or Metal Organic Chemical Vapor Deposition (MOCVD) on silicon faces for the moment problems related to the lattice mismatch which generates defects. We can therefore look at the side of transfer techniques such as lift-off and wafer bonding, or consider new low temperature growth methods such as Plasma Enhanced Atomic Layer Deposition (PE-ALD) [40]. Another possibility is the combination with perovskites, and the interface compatibility work has to be carried out. In particular, it will be necessary to study which type of Electron Transport Materials (ETM) or Hole Transport Materials (HTM) layer could also play the role of SL layer and make the selectivity at the heterointerface with silicon.

Acknowledgment

This work has been supported by the French National Research Agency (ANR) under the THESIS contract of the “Appel à projets générique 2018 CE05 - Une énergie durable, propre, sûre et efficace” program.

Reference

[1] K. Yoshikawa, H. Kawasaki, W. Yoshida, T. Irie, K. Konishi, K. Nakano, T. Uto, D. Adachi, M. Kanematsu, H. Uzu and K. Yamamoto, "Silicon heterojunction solar cell with interdigitated back contacts for a photoconversion efficiency over 26%", Nature Energy 2, 17032 (2017)

[2] W. Shockley and H. J. Queisser, "Detailed Balance Limit of Efficiency of p-n Junction Solar Cells", J. Appl. Phys. 32, 510 (1961).

[3] M. J. Kerr, A. Cuevas, P. Campbell. "Limiting efficiency of crystalline silicon solar cells due to Coulomb-enhanced Auger recombination", Progress In Photovoltaics: Research and Applications 11, 97 (2003) (DOI: 10.1002/pip.464).

[4] M. A. Green, Y. Hishikawa, W. Warta, E. D. Dunlop, D. H. Levi, J. Hohl-Ebinger, A. W.Y. Ho-Baillie, "Solar cell efficiency tables (version 50)", Prog Photovolt Res Appl. 25, 668 (2017)

[5] E. L. Warren, M. G. Deceglie, M. Rienäcker, R. Peibst, A. C. Tamboli, P. Stradins, "Maximizing tandem solar cell power extraction using a three-terminal design", Sustainable Energy & Fuels, 2, 1141 (2018)
[6] R. R. King, a. Boca, W. Hong, X. Q. Liu, D. Bhusari, D. Larrabee, K. M. Edmondson, D. C. Law, C. M. Fetzer, S. Mesropian, and N. H. Karam, "Band-gap-engineered architectures for high-efficiency multijunction concentrator solar cells acknowledgments", in 24th Eur. Photovolt. Sol. Energy Conf., Hamburg, Germany (2009), pp. 55 – 61.
[7] T. S. C. Takamoto, H. Washio, and H. Juso, "Application of InGaP / GaAs / InGaAs triple Junction Solar cells to Space Use and Concentrator Photovoltaic", in 2014 IEEE 40th Photovoltaic Specialist Conference (PVSC) (2014), pp. 1–5.
[8] J. P. Connolly, D. Mencaraglia, C. Renard, and D. Bouchier, "Designing III-V multijunction solar cells on silicon", Prog. Photovolt: Res. Appl. 22, 810 (2014).
[9] A. De Vos, "Detailed balance limit of the efficiency of tandem solar cells", J. Phys. D. Appl. Phys. 13, 839 (1980).
[10] Press release: Alta Devices Achieves "31.6% Solar Energy Efficiency Record; Changes the Fundamental Economics for Unmanned Aerial Vehicles", Apr. 2016.
[11] F. Dimroth, T. Roesener, S. Essig, C. Weuffen, A. Wekkeli, E. Oliva, G. Siefer, K. Volz, T. Hannappel, D. Haussler, W. Jager, and A. W. Bett, "Comparison of direct growth and wafer bonding for the fabrication of GaInP/GaAs dual-junction solar cells on silicon", IEEE J. Photovoltaics 4, 620 (2014).
[12] K. Tanabe, K. Watanabe, and Y. Arakawa, "III-V/Si hybrid photonic devices by direct fusion bonding", Sci. Rep. 2: 349 (2012).
[13] Romain Cariou, Jan Benick, Paul Beutel, Nasser Razek, Christoph Flötgen, Martin Hermle, David Lackner, Stefan W. Glunz, Andreas W. Bett, Markus Wimplinger, and Frank Dimroth, "Monolithic Two-Terminal III–V//Si Triple-Junction Solar Cells With 30.2% Efficiency Under 1-Sun AM1.5g", IEEE J. Phot. 7, 367 (2017).
[14] L. Reichertz and I. Gherasoiu, "Progress on III-nitride/silicon hybrid multijunction solar cells", in 2010 IEEE 35th Photovoltaic Specialist Conference (PVSC) (2010), pp. 1044–1047.
[15] Kevin A. Bush, Axel F. Palmstrom, Zhengshan J. Yu, Mathieu Boccard, Rongrong Cheacharoen, Jonathan P. Mailoa, David P. McMeekin, Robert L. Z. Hoye, Colin D. Bailie, Tomas Leijtens, Ian Marius Peters, Maxmillian C. Minichetti, Nicholas Rolston, Rohit Prasanna, Sarah Sofia, Duncan Harwood, Wen Ma, Farhad Moghadam, Henry J. Snaith, Tonio Buonassisi, Zachary C. Holman, Stacey F. Bent & Michael D. McGehee, "23.6%-efficient monolithic perovskite/silicon tandem solar cells with improved stability", Nat. Energy 2: 17009 (2017).
[16] H. Liu, Z. Ren, Z. Liu, A. G. Aberle, T. Buonassisi, and I. M. Peters, "The realistic energy yield potential of GaAs-on-Si tandem solar cells: a theoretical case study", Opt. Express 23, A382 (2015)
[17] J. Yang and R. Kleiman, "Optimization of bonded III-V on Si multi-junction solar cells," *in Conf. Rec. IEEE Photovolt. Spec. Conf.*, pp. 2151–2153 (2013).
[18] S. Essig, C. Allebé, T. Remo, J. F. Geisz, M. A. Steiner, K. Horowitz, L. Barraud, J. S. Ward, M. Schnabel, A. Descoeudres, D. L. Young, M. Woodhouse, M. Despeisse, C. Ballif, and A. Tamboli, "Raising the one-sun conversion efficiency of III–V/Si solar cells to 32.8% for two junctions and 35.9% for three junctions", Nat. Energy 2:,17144 (2017).
[19] J. Werner, L. Barraud, A. Walter, M. Bräuninger, F. Sahli, D. Sacchetto, N. Tétreault, B. Paviet-Salomon, S.-J. Moon, C. Allebé, M. Despeisse, S. Nicolay, S. D. Wolf, B. Niesen, and C. Ballif, "Efficient Near-Infrared-Transparent Perovskite Solar Cells Enabling Direct Comparison of 4-Terminal and Monolithic Perovskite/Silicon Tandem Cells", ACS energy Lett. 1, 474 (2016).
[20] T. Nagashima, K. Okumura, K. Murata and Y. Kimura, "Three-terminal tandem solar cells with a back-contact type bottom cell", Proc. 28th IEEE Photovoltaic Specialists Conference (2000), pp. 1193-1196.
[21] T. Nagashima, K. Hokoi, K. Okumura and M. Yamaguchi, "Surface passivation for germanium and silicon back contact type photovoltaic cells", Proc. 4th World Conference on Photovoltaic Energy Conference, (2006), pp. 655–658

[22] J. C. Jimeno, R. Gutierrez, V. Fano, A. Habib, C. del Cañizo, M. A.Rasool, A. Otaegi, " A 3 terminal parallel connected silicon tandem solar cell", Energy Procedia 92, 644 (2016).
[23] A. Martı and A. Luque, “Three-terminal heterojunction bipolar transistor solar cell for high-efficiency photovoltaic conversion”, *Nature communications* 6: 6902 (2015).
[24] G. W. P. Adhyaksa , E. Johlin, and E. C. Garnett, “Nanoscale Back Contact Perovskite Solar Cell Design for Improved Tandem Efficiency”, Nano Lett. 17, 9, 5206-5212 (2017).
[25] Z. Djebbour, W. El-Huni, A. Migan and J-P. Kleider "Photovoltaic Cell", Patent of International publication number: WO 2017/093695.
[26] I. Almansouri, A. Ho-Baillie, S.P. Bremner, and M.A. Green, "Supercharging silicon solar cell performance by means of multijunction concept", IEEE J. Photovoltaics 5(3), 968 (2015).
[27] S. Adachi, "Optical dispersion relations for GaP, GaAs, GaSb, InP, InAs, InSb, $Al_xGa_{1-x}As$, and $In_{1-x}Ga_xAs_yP_{1-y}$", J. Appl. Phys. **66**, 6030 (1989)
[28] D. M. Caughey and R. E. Thomas "Carrier Mobilities in Silicon Empirically Related to Doping and Field", Proc. IEEE 55, 2192 (1967).
[29] M. E. Law, E. Solley, M. Liang, D. E. Burk, "Self-consistent model of minority-carrier lifetime, diffusion length, and mobility", IEEE Electron Dev. Lett. 12, 401 (1991)
[30] J.G. Fossum, D.S. Lee, "A physical model for the dependence of carrier lifetime on doping density in nondegenerate silicon", Solid-State Electronics 25, 741 (1982)
[31] I. Vurgaftman, J.R. Meyer, L.R. Ram-Mohan, "Band parameters for III–V compound semiconductors and their alloys" J. Appl. Phys. 89, 5815 (2001). https://doi.org/10.1063/1.1368156
[32] IOFFE Physico-Technical Institute, http://www.ioffe.ru/SVA/NSM/Semicond/index. html
[33] L. Guijiang, W. Jyhchiarng and H. Meichun. "Theoretical modeling of the interface recombination effect on the performance of III–V tandem solar cells" Journal of Semiconductors, 31, 8 (2010) **DOI:** 10.1088/1674-4926/31/8/082004
[34] M.Y. Ghannam, J. Poortmans, J.F. Nijs, R.P. Mertens. "Theoretical study of the impact of bulk and interface recombination on the performance of GaInP/GaAs/Ge triple junction tandem solar cells. Photovoltaic Energy Conversion", Proceedings of 3rd World Conference, pp:666 - 669 Vol.1 (2003).
[35] S. Adachi, "Physical Properties of III-V Semiconductor Compounds InP, InAs, GaAs, GaP, InGaAs, and InGaAsP" New York: John Wiley and Sons, 1992.
[36] E. Franklin, K. Fong, K. McIntosh, A. Fell, A. Blakers, T. Kho, D. Walter, D. Wang, N. Zin, M. Stocks, E-C. Wang, N. Grant, Y. Wan, Y. Yang, X. Zhang, Z. Feng and P-J. Verlinden, "Design, fabrication and characterisation of a 24.4% efficient interdigitated back contact solar cell", Progress In Photovoltaics: Research and Applications 24(4), 411 (2014). DOI: 10.1002/pip.2556.
[37] W. El-Huni, A. Migan, Z. Djebbour, J-P. Salvestrini and A. Ougazzaden, "High-efficiency InGaN/Si tandem photovoltaic solar cells modelling using InGaN semibulk material: monolithic integration vs. 4-terminals tandem cells", Progress in Photovoltaic: Research and Application, (2016), published on line, DOI: 10.1002/pip.2807.
[38] C.R. Allen, J.M. Woodall, J.-H. Jeon, "Results of a gallium phosphide photovoltaic junction with an AR coating under concentration of natural sunlight", Solar Energy Materials & Solar Cells 95 (2011) 2655–2658
[39] J. F. Geisz, M. A. Steiner, I. García, S. R. Kurtz, and D. J. Friedman, "Enhanced external radiative efficiency for 20.8% efficient single-junction GaInP solar cells", Appl. Phys. Lett. **103**, 041118 (2013).
[40]A-S. Gudovskikh, I-A. Morozov, A-V. Uvarov, D-A. Kudryashov, E-V. Nikitina, A-A. Bukatin, V. Nevedomskiy, J-P. Kleider, "*Low temperature plasma enhanced atomic layer deposition of GaP films on Si substrate*", J. Vac. Sci. Tech. A : Vacuum, Surfaces, and Films 36 (2018) 021302, DOI : 10.1116/1.4999409.

***Table 1**: Physical parameters of the FHS*

Parameter	Expression or value
$Ga_xIn_{1-x}P$ bandgap (eV) [31]	$E_g = \begin{cases} 2.86x + 1.423(1-x) - 0.65x(1-x) & x < 0.7\ (Direct) \\ 2.35x + 2.38(1-x) - 0.2x(1-x) & x > 0.7\ (Indirect) \end{cases}$
$Ga_xIn_{1-x}P$ electron affinity (eV) [32]	$\chi = 4.38 - 0.58x$
Absorption coefficient [33] $(\boldsymbol{10^4 cm^{-1}})$	$\alpha_{Ga_xIn_{1-x}P} = 5.5\sqrt{E - E_g} + 1.5\sqrt{E - E_g - 1}$
Carrier lifetime [34]	$1/\tau_{p,n} = 1/\tau_{SRH} + B \cdot N_{total}$ where $\tau_{SRH} = 10\ \mu s$, $B = 7.5\ 10^{-10} cm^3 s^{-1}$ $N_{total} = \begin{cases} N_a = 2 \cdot 10^{18} cm^{-3} & (p - GaP) \\ N_d = 10^{14} cm^{-3} & (i - GaInP) \end{cases}$
Carrier mobility [34]	$\mu_n = 4000\ cm^2 V^{-1} s^{-1}$; $\mu_p = 40\ cm^2 V^{-1} s^{-1}$
Refractive index [35]	Adachi's dispersive model has been used

***Table 2**: IBC cell* [36] and GaN [37] *device and layers parameters*

Parameter	Si	GaN
Bandgap	1.1 eV	3.4 eV
Electron affinity	4.17 eV	4.2 eV
$\boldsymbol{\tau_{n_0}^{SRH} = \tau_{p_0}^{SRH}}$	$5\ ms$	$1\ ns$
Absorber n-type doping	$2 \cdot 10^{15}\ cm^{-3}$	$1 \cdot 10^{14}\ cm^{-3}$
Contact n^+ doping	$1 \cdot 10^{20}\ cm^{-3}$	
Contact p^+ doping	$5 \cdot 10^{19}\ cm^{-3}$	
SRV at metal contacts	$10^5 cms^{-1}$	
$\boldsymbol{A_n = A_p}$	1	1
$\boldsymbol{B_n = B_p}$	1	1
$\boldsymbol{C_n = C_p}$	0	0
$\boldsymbol{E_n}$	Not necessary: $C_n = 0$	
$\boldsymbol{E_p}$	Not necessary: $C_p = 0$	
$\boldsymbol{N_n^{SRH} = N_p^{SRH}}$	$5 \cdot 10^{16}\ cm^{-3}$	
$\boldsymbol{C_{Aug}^n}$	$2.8 \cdot 10^{-31}\ cm^{-3}/s$	
$\boldsymbol{C_{Aug}^p}$	$9.9 \cdot 10^{-32}\ cm^{-3}/s$	
$\boldsymbol{\mu_{1_n}}$	$55.24\ cm^2 V^{-1} s^{-1}$	$55\ cm^2 V^{-1} s^{-1}$
$\boldsymbol{\mu_{1_p}}$	$49.7\ cm^2 V^{-1} s^{-1}$	$3\ cm^2 V^{-1} s^{-1}$
$\boldsymbol{\mu_{2_n}}$	$1429.23\ cm^2 V^{-1} s^{-1}$	$1000\ cm^2 V^{-1} s^{-1}$
$\boldsymbol{\mu_{2_p}}$	$479.37\ cm^2 V^{-1} s^{-1}$	$170\ cm^2 V^{-1} s^{-1}$
$\boldsymbol{N_n^{ref}}$	$1.07 \cdot 10^{17}\ cm^{-3}$	$2 \cdot 10^{17}\ cm^{-3}$
$\boldsymbol{N_p^{ref}}$	$1.6 \cdot 10^{17}\ cm^{-3}$	$2 \cdot 10^{17}\ cm^{-3}$
$\boldsymbol{\delta_n}$	0.73	1
$\boldsymbol{\delta_p}$	0.7	2

***Table 3**: Calculated photovoltaic performance (short circuit current density, J_{SC}, open circuit voltage, V_{OC}, fill factor, FF, power conversion efficiency, PCE) under AM 1.5 illumination of our subcells and comparison to literature data.*

Structure	J_{sc} (mA/cm^2)	V_{OC} (mV)	FF (%)	PCE (%)
Our GaInP/Si subcell	16.7	1170	86.4	16.8
record GaInP cell from ref. [38]	16.0	1450	89.3	20.8
Our n-Si IBC subcell	36.56	704.0	83.3	21.5
IBC from ref. [36]	41.95	702.5	82.7	24.4

Figure captions

Figure 1*: General FHS/SL/c-Si three-terminals tandem cells based on either n-type (a) or p-type (b) crystalline silicon absorber interdigitated back contact cell.*

Figure 2*: Sketch of the simulated subcells: (a) the GaInP/n-Si heterojunction vertical top cell, and (b) the n-Si IBC cell.*

Figure 3: *(a) Sketch of the structure without SL chosen to illustrate the working principle and performance of the 3-T architecture on an n-type silicon wafer. The p-FHS stack consists of an undoped i-$Ga_{0.35}In_{0.65}P$ absorber layer, a thin graded bandgap i-GaInP adaptative layer and a top p-GaP front layer. (b) The corresponding energy band diagram at equilibrium of the chosen III-V stack on n-type silicon without SL layer. The combination of the front p-GaP, graded i-GaInP, and i-$Ga_{0.35}In_{0.65}P$ layers on n-type Si produce a p-i-n heterojunction.*

Figure 4*: Electrons current mapping in the whole tandem solar cell under AM1.5G in the short-circuit configuration (for both subcells) (a), and its zoom-in close to the InGaP/Si heterointerface (b). Arrows indicate the conventional sense of current, the flow of electrons being in the opposite direction.*

Figure 5*: Holes current mapping in the whole 3-T tandem solar cell under AM1.5G in the short-circuit configuration (for both subcells) (a) and its zoom-in close to the InGaP/Si heterointerface (b). Arrows indicate the conventional sense of current, the flow of holes being in the same direction.*

Figure 6: *Sketch of the BESTT structure integrating the SL layer (a), and energy band diagram at equilibrium across the top layers and the heterointerface with n-Si (b). The SL consists in a 150 nm thick GaN layer, the p-FHS stack consists of an undoped i-$Ga_{0.35}In_{0.65}P$ absorber layer, a thin graded bandgap i-GaInP adaptative layer and a top p-GaP front layer. The thicknesses of the layers have been optimized by the simulation.*

Figure 7*: Holes current mapping at the SL/Si interface (a), and the total photocurrent mapping in the whole 3-T tandem solar cell under AM1.5 in the short-circuit conditions.*

Figure 8*: Mapping of the power conversion efficiency of the BESTT cell with PMMA anti-reflecting coating, with respect to the top and the bottom cell operation point voltages, without SL layer (structure of Figure 3a) (a), and with a GaN SL layer (structure of Figure 6a) (b).*

Figure 9*: Current-voltage characteristics under AM 1.5G of the top (a) and bottom (b) subcell for various operating points of the bottom and top subcell, respectively. Simulations have been performed with the structure of Figure 3a without SL.*

Figure 10*: Energy band diagram profiles under AM1.5G for two operating points of the bottom cell while the top cell is at open-circuit (a) and for two operating points of the top cell while the bottom cell is in short circuit (b). The profile corresponds to a vertical line joining the upper p-electrode and the bottom n-electrode, as indicated by the dashed-dotted line in the inserts.*

Figure 11: *Current-voltage characteristics under AM 1.5G of the top (a) and bottom (b) subcell for various operating points of the bottom and top subcell, respectively. Simulations have been performed with the structure of Figure 6a using the SL layer.*

***Figure 12**: Photovoltaic performance of the InGaP / Si hetero-tandem BESTT cell, (a) without SL layer and (b) with SL layer. In the latter case, the I-V characteristics of the subcells are fully independent one another.*

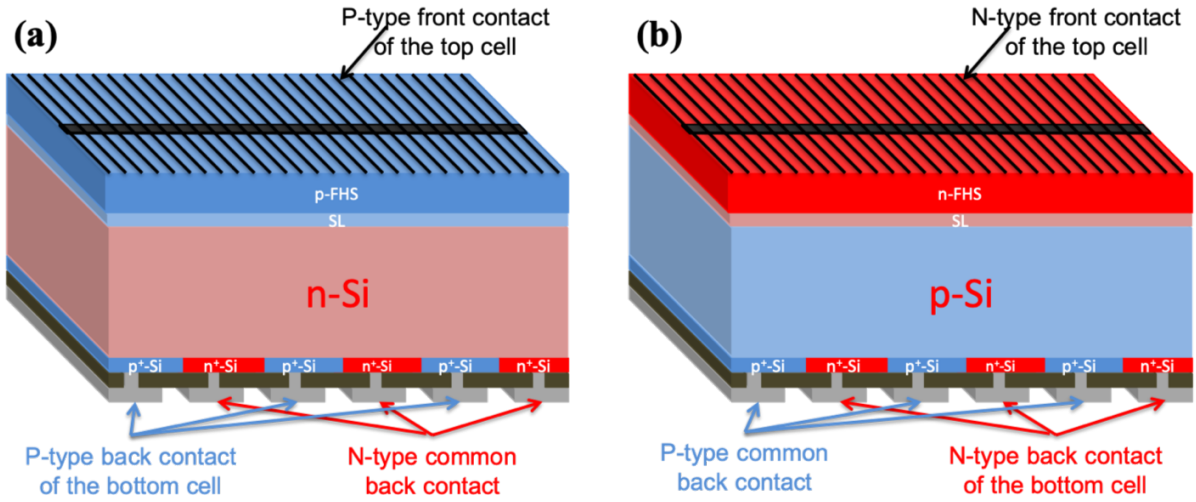

***Figure 1**: General FHS/SL/c-Si three-terminals tandem cells based on either n-type (a) or p-type (b) crystalline silicon absorber interdigitated back contact cell.*

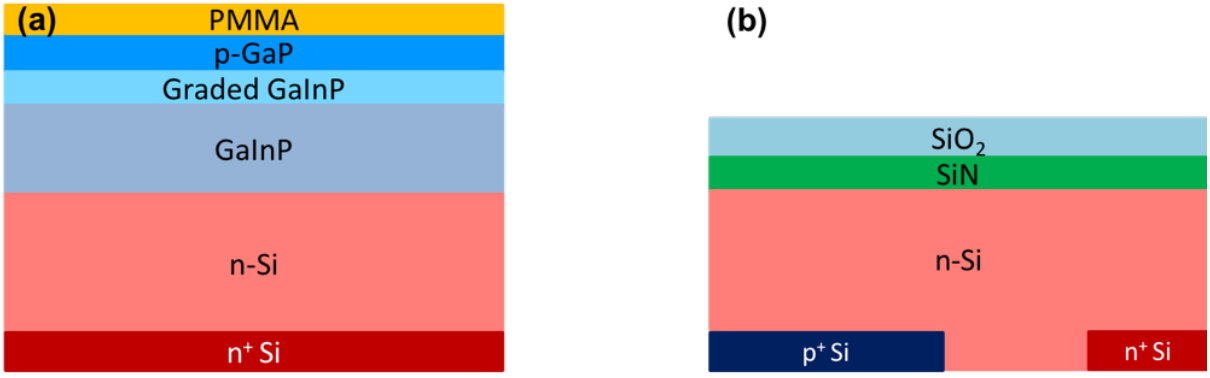

***Figure 2**: Sketch of the simulated subcells: (a) the GaInP/n-Si heterojunction vertical top cell, and (b) the n-Si IBC cell.*

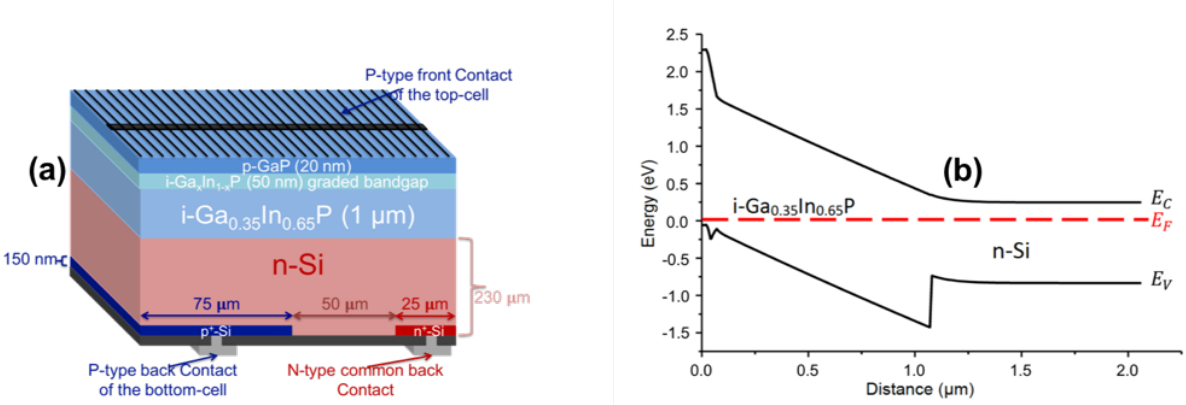

***Figure 3:** (a) Sketch of the structure without SL chosen to illustrate the working principle and performance of the 3-T architecture on an n-type silicon wafer. The p-FHS stack consists of an undoped i-$Ga_{0.35}In_{0.65}P$ absorber layer, a thin graded bandgap i-GaInP adaptative layer and a top p-GaP front layer. (b) The corresponding energy band diagram at equilibrium of the chosen III-V stack on n-type silicon without SL layer. The combination of the front p-GaP, graded i-GaInP, and i-$Ga_{0.35}In_{0.65}P$ layers on n-type Si produce a p-i-n heterojunction.*

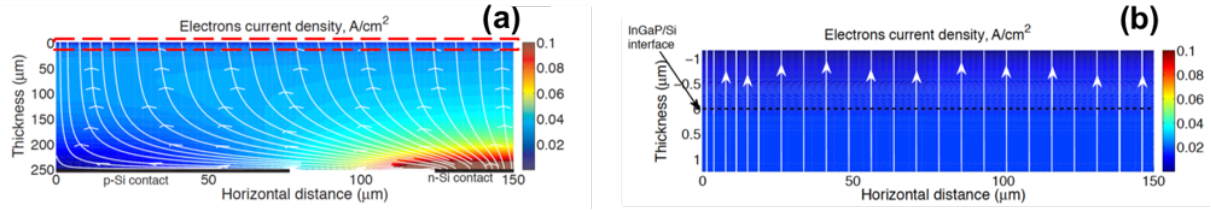

***Figure 4**: Electrons current mapping in the whole tandem solar cell under AM1.5G in the short-circuit configuration (for both subcells) (a), and its zoom-in close to the InGaP/Si heterointerface (b). Arrows indicate the conventional sense of current, the flow of electrons being in the opposite direction.*

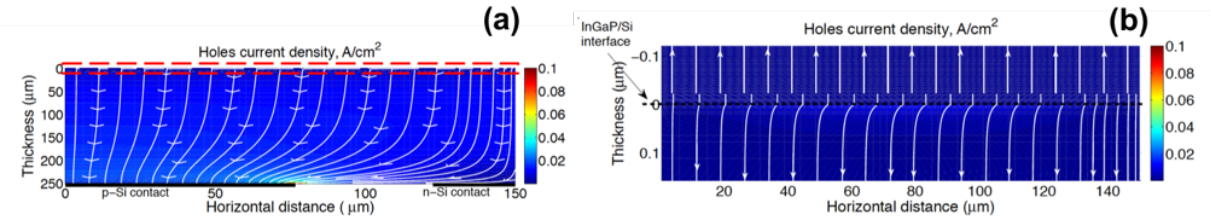

***Figure 5**: Holes current mapping in the whole 3-T tandem solar cell under AM1.5G in the short-circuit configuration (for both subcells) (a) and its zoom-in close to the InGaP/Si heterointerface (b). Arrows indicate the conventional sense of current, the flow of holes being in the same direction.*

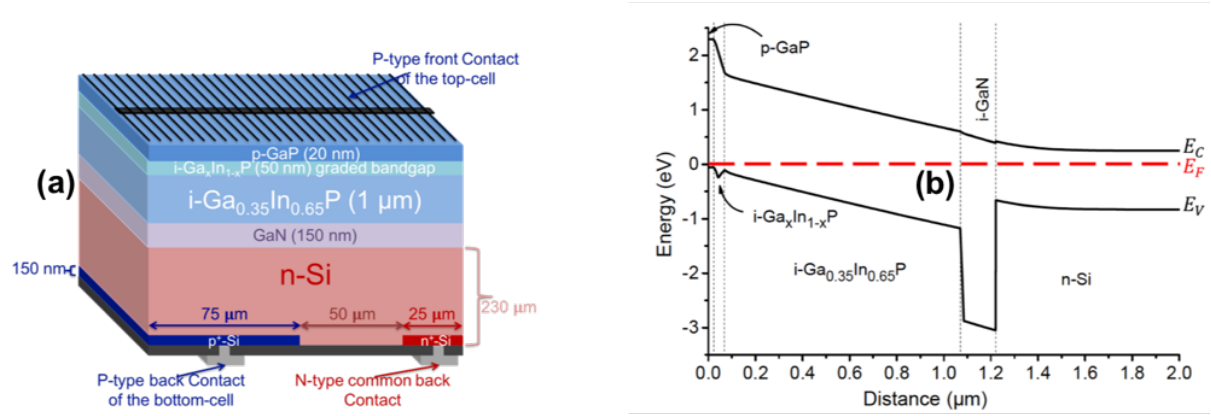

***Figure 6:** Sketch of the BESTT structure integrating the SL layer (a), and energy band diagram at equilibrium across the top layers and the heterointerface with n-Si (b). The SL consists in a 150 nm thick GaN layer, the p-FHS stack consists of an undoped i-$Ga_{0.35}In_{0.65}P$ absorber layer, a thin graded bandgap i-GaInP adaptative layer and a top p-GaP front layer. The thicknesses of the layers have been optimized by the simulation.*

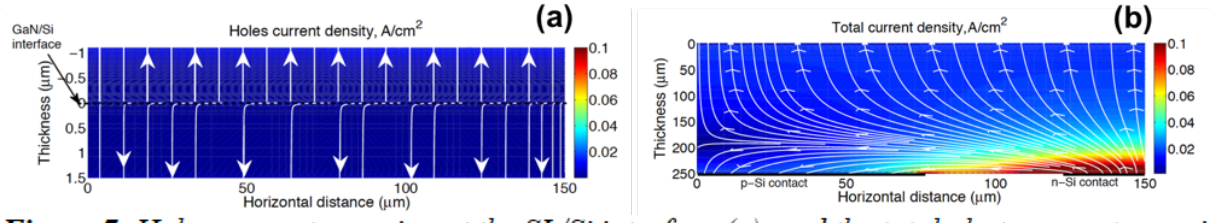

***Figure 7**: Holes current mapping at the SL/Si interface (a), and the total photocurrent mapping in the whole 3-T tandem solar cell under AM1.5 in the short-circuit conditions.*

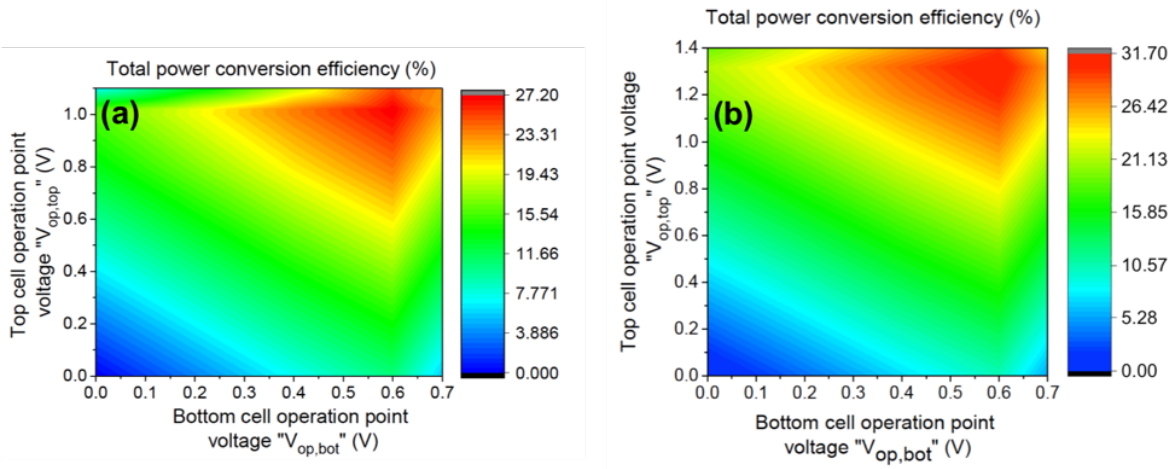

***Figure 8**: Mapping of the power conversion efficiency of the BESTT cell with PMMA anti-reflecting coating, with respect to the top and the bottom cell operation point voltages, without SL layer (structure of Figure 3a) (a), and with a GaN SL layer (structure of Figure 6a) (b).*

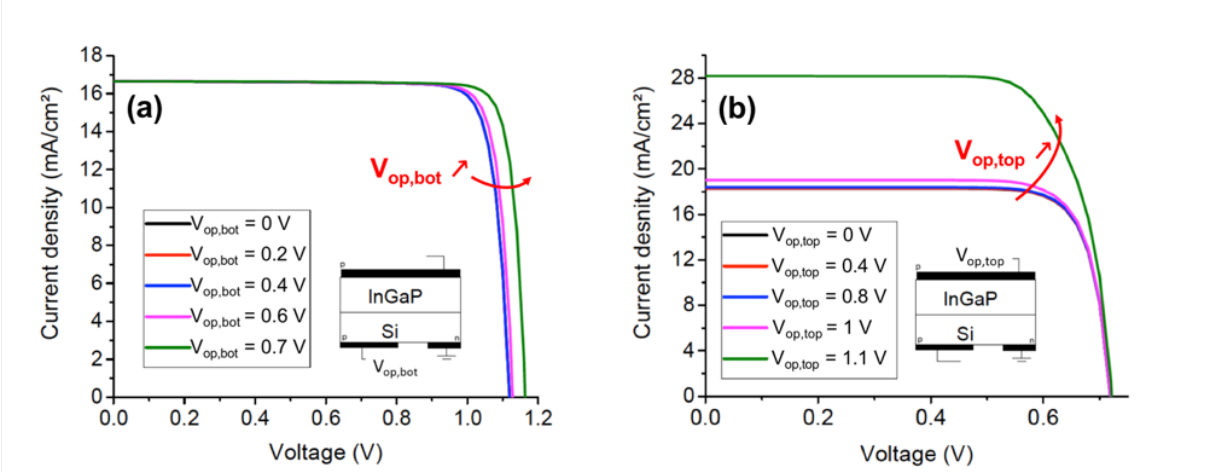

***Figure 9**: Current-voltage characteristics under AM 1.5G of the top (a) and bottom (b) subcell for various operating points of the bottom and top subcell, respectively. Simulations have been performed with the structure of Figure 3a without SL.*

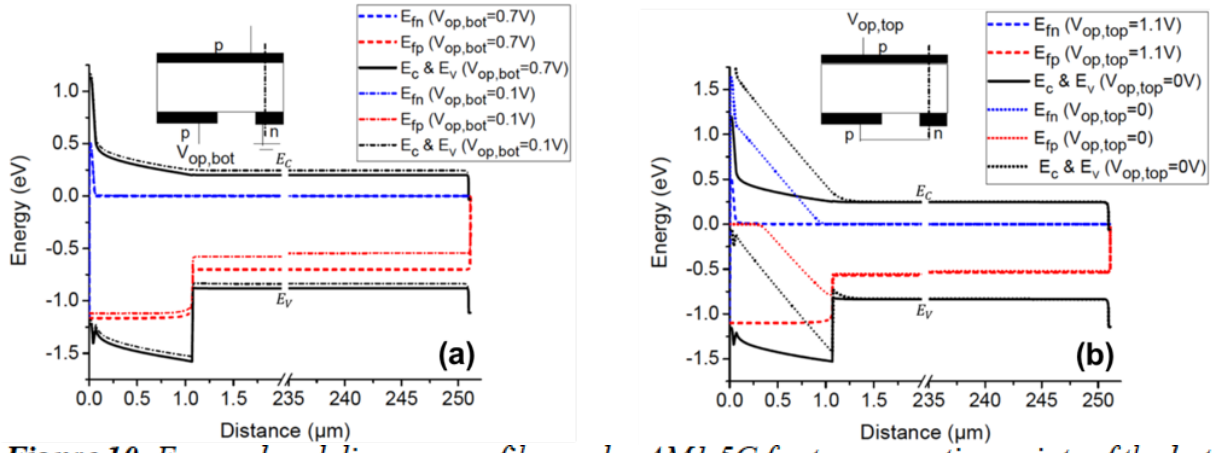

***Figure 10**: Energy band diagram profiles under AM1.5G for two operating points of the bottom cell while the top cell is at open-circuit (a) and for two operating points of the top cell while the bottom cell is in short circuit (b). The profile corresponds to a vertical line joining the upper p-electrode and the bottom n-electrode, as indicated by the dashed-dotted line in the inserts.*

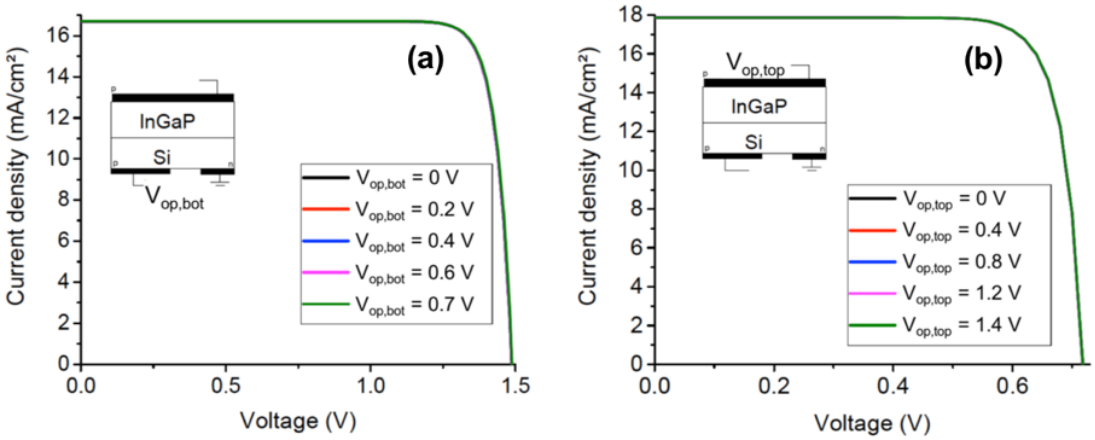

Figure 11: *Current-voltage characteristics under AM 1.5G of the top (a) and bottom (b) subcell for various operating points of the bottom and top subcell, respectively. Simulations have been performed with the structure of Figure 6a using the SL layer.*

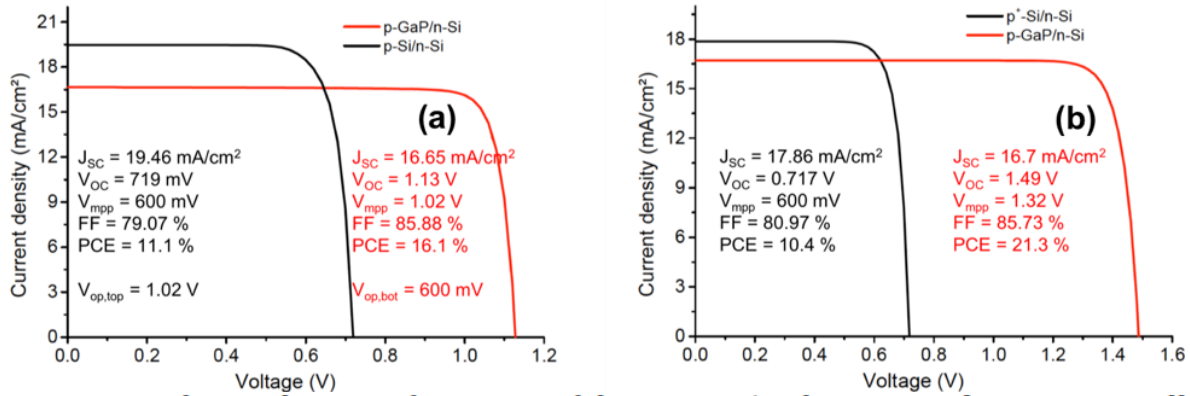

Figure 12*: Photovoltaic performance of the InGaP / Si hetero-tandem BESTT cell, (a) without SL layer and (b) with SL layer. In the latter case, the I-V characteristics of the subcells are fully independent one another.*